

# ScoreNet: Learning Non-Uniform Attention and Augmentation for Transformer-Based Histopathological Image Classification

Thomas Stegmüller<sup>1</sup> Antoine Spahr<sup>1</sup> Behzad Bozorgtabar<sup>1,2,3</sup> Jean-Philippe Thiran<sup>1,2,3</sup>  
<sup>1</sup>EPFL, Switzerland <sup>2</sup>CHUV, Switzerland <sup>3</sup>CIBM, Switzerland  
 {firstname.lastname}@epfl.ch

## Abstract

Progress in digital pathology is hindered by high-resolution images and the prohibitive cost of exhaustive localized annotations. The commonly used paradigm to categorize pathology images is patch-based processing, which often incorporates multiple instance learning (MIL) to aggregate local patch-level representations yielding image-level prediction. Nonetheless, diagnostically relevant regions may only take a small fraction of the whole tissue, and MIL-based aggregation operation assumes that all patch representations are independent and thus mislays the contextual information from adjacent cell and tissue microenvironments. Consequently, the computational resources dedicated to a specific region are independent of its information contribution. This paper proposes a transformer-based architecture specifically tailored for histopathological image classification, which combines fine-grained local attention with a coarse global attention mechanism to learn meaningful representations of high-resolution images at an efficient computational cost. More importantly, based on the observation above, we propose a novel mixing-based data-augmentation strategy, namely ScoreMix, by leveraging the distribution of the semantic regions of images during the training and carefully guiding the data mixing via sampling the locations of discriminative image content. Thorough experiments and ablation studies on three challenging representative cohorts of Haematoxylin & Eosin (H&E) tumour regions-of-interest (TRoIs) datasets have validated the superiority of our approach over existing state-of-the-art methods and effectiveness of our proposed components, e.g., data augmentation in improving classification performance. We also demonstrate our method's interpretability, robustness, and cross-domain generalization capability.

## 1. Introduction

Due to the increasing availability of digital slide scanners enabling pathologists to capture sizable high-resolution

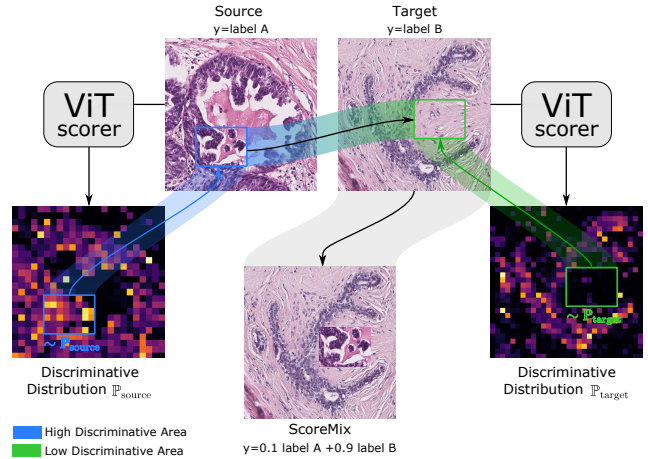


Figure 1. A **ScoreMixed** training pair  $(x_m, y_m)$  is produced by pasting a region of high semantic content from the source image,  $x_s$ , in the target image  $x_t$  and obtaining a convex combination of the labels. The distribution of the semantic content is learnable and computed on-the-fly.

whole slide images (WSI), computational pathology has recently witnessed a lot of advances, making this field a ripe ground for deep learning. Nonetheless, the diagnosis from H&E stained WSIs remains challenging. The difficulty of the task is a consequence of two inherent properties of histopathology image datasets: *i*) the huge size for images and *ii*) the cost of exhaustive localized annotations, making the usage of most deep learning models computationally infeasible. Patch-based processing approaches [14, 22, 30] have become a *de facto* practice for high dimensional pathology images that aggregate individual patch representation/classification predictions by, e.g., a convolutional neural network (CNN) for image-level prediction. Nonetheless, patch-based methods increase the requirement of patch-level labeling and further regions of interest (RoI) detection as diagnostic-related tissue sections might only take a small fraction of the whole tissue, leading to considerable uninformative patches. Prior CNN methods [15, 19] have adopted multiple instance learning (MIL) [21] to ad-

dress the above issues, which incorporates an attention-based aggregation operator to identify tissue sub-regions of high diagnostic value automatically. However, these methods assume that all the instances of patches are independent, which may not hold in practice and thus fail to fully capture the contextual information and the correlation information between different tissue sub-regions.

Recently, self-supervised learning (SSL) methods [18, 19, 31] aim to construct semantically meaningful visual representations via pretext tasks for histopathological images. Despite their notable success using the CNN backbones in improving classification performances, CNN’s receptive field often restricts the learning of global context features. In another line of research, to compensate for the lack of diverse and large datasets, data mixing-based augmentation techniques [34, 37, 37] have been developed to further enhance the performance of classification models. While there have been substantial gains for classification tasks on natural image datasets, we argue that such data augmentations may not be helpful for histopathological images, yielding to learn unexpected feature representation. Latterly, despite CNNs, vision transformer (ViT) models [11, 33] provide flexibility in capturing long-range visual dependencies due to their flexible receptive fields via self-attention mechanisms. More recently, self-supervised ViTs method [20, 35] combine the advantages of ViT and SSL to learn visual representations from less curated pre-training data efficiently. However, there is relatively little research on the impact of data augmentation design, efficiency and robustness of ViT, and patch token selection despite their usefulness. For example, *can we train a robust transformer network efficiently by selecting only informative regions of high diagnostic value (RoIs) from high-resolution images? What data augmentation strategies can improve the transformer’s representation learning for TRoIs classification?* This paper addresses these questions by uncovering insights about key aspects of data augmentation and image non-uniformly representation used to train transformers.

**Contributions.** Our contributions are as follows:

1. We propose a transformer-based architecture specifically tailored for histopathological image classification. It combines fine-grained local attention with a coarse global attention mechanism to learn meaningful representations of high-resolution images at an efficient computational cost. Our proposed architecture is specifically tailored to be modular, thereby allowing for a dedicated self-supervised pre-training of the sub-parts of the model, which in return translates to competitive performance even with reduced labeled data;
2. We propose a novel mixing-based data-augmentation, namely ScoreMix for histopathological images.

ScoreMix works in synergy with our architecture, as they build upon the same observation: the different regions of the images are not equally relevant for a given task. Using learned self-attention for [CLS] token of the ViT, we determine the distribution of the semantic regions of images during the training to ensure that we sample the locations of discriminative content (RoI) for the cutting and pasting regions (see Fig. 1);

3. Benefiting the above contributions, we conducted various experiments on three challenging H&E cohorts of TRoIs. We achieved consistent improvements and faster convergence over existing state-of-the-art methods on the *BRACS* dataset while demonstrating our method’s interpretability and cross-domain generalization capability on the *CAMELYON16* and *BACH* datasets.

## 2. Related work

**TRoIs Classification.** Conventionally, deep learning methods [14, 22, 29, 30, 36] process pathology images in a patch-wise manner using a MIL formulation [21] and aggregate the patch-level features extracted by a CNN. Nonetheless, CNNs operate on fixed field-of-view, and thereby disregard the global context and the inter-patches interactions. These methods also treat all instances (patch-level features) identically, and the computational resources dedicated to a specific region are independent of its . Some prior methods [15, 19] proposed attention-based aggregation operators through trainable attention weights. However, the applicability of these methods is limited in practice as they often neglect tissue-level context and correlation information between different sub-regions. In another contemporary work, the attention-based MIL technique [16] has been proposed to process only representative patches extracted by an external tool [17] before further feature extraction by CNN. Therefore their patch extraction is fixed and not data-driven as ours. To cope with that loss of information, graph neural network-based methods [26, 39] have been proposed to consider global contextual information and the dependencies between the instances. These approaches build a graph model that operates on the cell-level structure or combines the cell-level and tissue-level context. However, graph generation can be cumbersome and computationally intensive despite good performances, prohibiting its use in real-time applications. Recently, SSL methods [18, 19, 31] have demonstrated their capabilities to improve classification for histopathological images. Most of these methods harness pretext tasks, e.g., contrastive pre-training, to learn semantically meaningful features. Nonetheless, the CNN backbone used in these approaches inevitably abandons learning of global context features. The transformer-based architecture

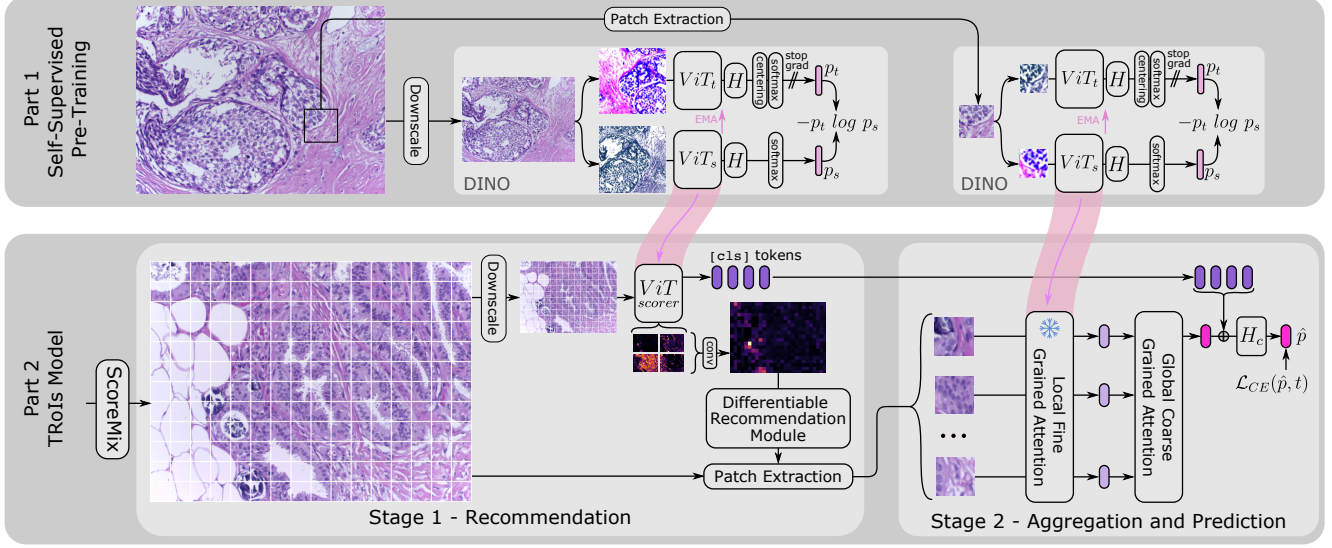


Figure 2. **An overview of the proposed ScoreNet.** (**Part 1**) Our modular architecture allows for a self-supervised ViT pre-training of constituent parts either on the downsampled images or on extracted patches. (**Part 2**) TRoIs classification pipeline is composed of two sub-modules: *Stage 1* details the dynamic selection of informative regions using the pre-trained ViT scorer, and *Stage 2* outlines the aggregation and prediction steps that process the discriminative regions using the fine-grained attention mechanism. The pink connections highlight the knowledge transfer between the two parts.  $H$  and  $H_c$  respectively denote the projection heads used in the self-supervised pre-training and the TRoIs classifier.

may be an alternative solution for processing images as a de-structured patch sequence and capturing their global dependencies. More recently, hybrid-based vision transformer models have been used in digital pathology [7, 28, 35], either based on MIL framework [28] or SSL pre-training [35] on unlabeled histopathological images. Nevertheless, these methods process the whole image uniformly and do not allow dynamic extraction of the region of interest.

**Mixing-Based Data-Augmentation Methods.** Recently, mixing-based data augmentations strategies [34, 37, 37] have been proposed to enhance the generalization and localization capabilities of deep network classifiers. These improvements are further exacerbated when the augmentations model the interactions between the classes [37]. These methods create a new augmented sample by cutting an image region from one image and pasting it on another image, while a convex combination of their labels gives the ground-truth label of the new sample. Despite the strong performances of the existing methods, none of them is genuinely satisfying as they either create samples that exhibit atypical local features as in MixUp [38] or produce potentially mislabeled samples as in CutMix [37]. CutMix assumes a uniform distribution of discriminative information on the images. However, this assumption may mislead the training and mislabel the samples. Closest to our approach are Attentive CutMix [34] and SaliencyMix [32] methods. The former requires an auxiliary pre-trained model to se-

lect the most salient patches from the source image before pasting them at the same location in the target image. Aside from the fact that this method only works with fixed-size images, it suffers from two main drawbacks: *i*) it disregards the location of the informative regions in the target image, and *ii*) by placing multiple disconnected patches, it forces the model to discard the shape information and to only base its predictions on the texture cues. SaliencyMix does not induce the same bias on the model as it processes bounding boxes rather than independent patches. Nonetheless, SaliencyMix assumes that discriminative parts in an image are highly correlated with the saliency map, which is typically not the case for histopathological images.

### 3. Method

**Model Overview.** In this section, we detail our proposed training pipeline for H&E stained histology TRoIs image classification, as summarized in Fig. 2. The training pipeline can be split into two different parts. Our modular architecture allows for a self-supervised ViT pre-training of constituent elements based on the recent self-labeling method, DINO [6], either on the downsampled images or extracted patches in **Part 1**. The learned ViT networks serve as the backbone of downstream (**Part 2**). The second part comprises several parts that dynamically extract image sub-regions (RoIs) of high diagnostic value through the proposed ScoreNet attention mechanism, which com-

bines fine-grained local attention with a coarse global attention mechanism at an efficient computational cost. The low-resolution image is fed to the first pre-trained ViT scorer network, which recommends RoIs to apply fine-grained attention (*Stage 1*). These regions are further used for the proposed upstream ScoreMix augmentation. Important regions within RoIs can then be extracted with a differentiable recommendation operator (*Stage 1*). Consequently, a coarse attention mechanism is applied to endow the locally attended regions with contextual information (*Stage 2*). To do so, the second pre-trained ViT is used as a potentially frozen feature extractor on the set of regions where to attend finely. The extracted features are then passed to a transformer encoder. Finally, the [CLS] token of the last transformer is merged with the [CLS] tokens of the first ViT in view of adding further global context information since the first ViT has seen the whole image. The resulting token is then passed through a projection head to obtain the final prediction.

### 3.1. Self-Supervised ViT Pre-Training

For our pre-training stage, we leverage a recent self-labeling ViT model DINO [6] that has shown sensible object segmentation ability using the self-attention of the [CLS] token. The model builds upon view-consistency learning between teacher-student networks, where the teacher network is fed with augmented large crops (global views) of the input image while the student network is fed with both augmented large and small crops (global and local views) of the same unlabeled image. The student network is updated to match the output (pseudo label) obtained from the teacher network  $p_t$  through the cross-entropy loss:  $\phi_s \leftarrow \min_{\phi_s} \mathcal{H}(s, t, \phi_s)$ , where  $\mathcal{H} = -p_t \log p_s$ , and  $p_s$  is the student's output. On the other side, the teacher network is updated by an exponential moving average (EMA) of the student's parameters:  $\phi_t \leftarrow \alpha \phi_t + (1 - \alpha) \phi_s$ , where  $\alpha \in [0, 1]$  is a hyper-parameter following a cosine schedule during training [6]. The student and the teacher have the same ViT architecture composed of a backbone feature extractor followed by a projection head.

### 3.2. TRoIs Model

Our modular TRoIs model is composed of two main stages. The first stage, implemented by a ViT [11], takes as input a downsampled image, and produces a sampling distribution over the high-resolution patches. The latter is obtained by observing that a ViT's self-attention map captures the contribution of each low-resolution patch to the overall representation, consequently it can be interpreted as a measure of the semantic relevance of each patch. The second stage, locally and independently, attends to each of the differentially selected high-resolution regions from *Stage 1* with a fine-grained attention module. Subsequently, the em-

bedded patches attend to one another (*coarse attention*) via a transformer encoder. The concatenation of the recommendation's stage [CLS] (s) and that of the *coarse attention*'s encoder produces the image's representation. Using the recommendation stage's [CLS] token(s) allows the model to capture shape information (see Sec. 4).

**Semantic Regions Recommendation.** Current MIL-based approaches [15, 19] based on patch-level features aggregation often process histopathological images uniformly and discard the inter-patches interactions. To alleviate these issues, our method relies on a **differentiable recommendation stage to extract discriminative image regions relevant for the classification**. We propose an approach that leverages the self-attention of a ViT as a distribution of the semantic content. Towards that end, the high-resolution image is first downsampled by a factor  $s$ , and subsequently fed to the recommendation's stage ViT. The resulting self-attention map captures the contribution of each patch to the overall representation.

Indeed, let us consider a ViT processing the low-resolution image  $x_l \in \mathbb{R}^{C \times h \times w}$  encompassing  $N$  patches of dimension  $P_l \times P_l$ . The attended patches or tokens of the  $(L - 1)$  layer are conveniently represented as a matrix  $\mathbf{Z} \in \mathbb{R}^{(N+1) \times d}$ , where  $d$  is the embedding dimension of the model, and the extra index is due to the [CLS] token. Up to the last MLP and for a single attention head, the representation of the complete image is given by:

$$y_{[\text{CLS}]} = \underbrace{\text{softmax}(a_1^T)}_{1 \times (N+1)} \underbrace{\mathbf{Z} \mathbf{W}_{\text{val}}}_{(N+1) \times d} \quad (1)$$

where  $\mathbf{W}_{\text{val}} \in \mathbb{R}^{d \times d}$  is the value matrix, and  $a_1^T$  is the first row of the self-attention matrix:

$$\mathbf{A} = \mathbf{Z} \mathbf{W}_{\text{qry}} (\mathbf{Z} \mathbf{W}_{\text{key}})^T \quad (2)$$

hence, the first row of the self-attention matrix captures the contribution of each token to the overall representation (Eq. 1). This is in line with the discriminative capacity of the [CLS] token, that the patches having the highest contribution are the ones situated in the highest semantic regions of the images. The distribution of the semantic content over the patches is therefore defined as:

$$\mathbb{P}_{\text{patch}} = \text{softmax}(\tilde{a}_1^T) \in \mathbb{R}^N \quad (3)$$

where  $\tilde{a}_1$  stands for  $a_1$  without the first entry, namely the one corresponding to the [CLS] token. In practice, ViTs typically encompass multiple heads, we propose to address this issue by adding an extra learnable parameter, which weighs the contribution of each head to the end task; after aggregation of the multiples self-attention maps, the formulation is identical to that of Eq. 3.



Concurrently to the obtention of the above defined semantic distribution, the high-resolution image,  $x_h \in \mathbb{R}^{C \times H \times W}$ , is tiled in a regular grid of large patches ( $P_h \times P_h$ ), stored in a tensor  $\mathbf{P} \in \mathbb{R}^{N \times C \times P_h \times P_h}$ . At inference time, a convenient way to extract the  $K$  most semantically relevant high-resolution regions is to encode the *top-K* indices as one-hot vectors:  $\mathbf{Y} \in \mathbb{R}^{N \times K}$ , and to extract the corresponding  $K$  patches,  $\mathbf{X} \in \mathbb{R}^{K \times C \times P_h \times P_h}$  via:

$$\mathbf{X} = \mathbf{Y}^T \mathbf{P} \quad (4)$$

At training time, one has to be more careful, as the above method is not differentiable and doesn't allow the recommendation stage to receive gradients. The differentiable approach of [9] is therefore adopted. Following the perturbed optimizers scheme, the *top-K* operation is bootstrapped by applying a Gaussian noise,  $\sigma \mathbf{Z}$ , to the semantic distribution. The noisy indicators,  $\mathbf{Y}_\sigma$ , are subsequently computed as:

$$\mathbf{Y}_\sigma = \mathbb{E}_{\mathbf{Z}} \left[ \arg \max_{\mathbf{Y} \in \mathcal{C}} \langle \mathbf{Y}, \tilde{\mathbf{P}} + \sigma \mathbf{Z} \rangle \right] \quad (5)$$

where  $\sigma$  is the standard deviation of the noise,  $\tilde{\mathbf{P}} \in \mathbb{R}^{N \times K}$  is obtained by broadcasting  $\mathbb{P}_{\text{patch}}$  to match the dimension of  $\mathbf{Y}$ , and  $\mathcal{C}$  is a restriction of the domain of admissible indicators,  $\mathbf{Y}$ , ensuring the equivalence between solving Eq. 5 and the *top-K* operation [9]. The extraction of the high-resolution regions follows the procedure described in Eq. 4. Similarly, the gradient of the indicators w.r.t. the semantic distribution,  $\mathbb{P}_{\text{patch}}$ , is:

$$\nabla \mathbf{Y}_\sigma = \mathbb{E}_{\mathbf{Z}} \left[ \arg \max_{\mathbf{Y} \in \mathcal{C}} \langle \mathbf{Y}, \tilde{\mathbf{P}} + \sigma \mathbf{Z} \rangle \mathbf{Z}^T / \sigma \right] \quad (6)$$

**Coarse and Fine-Grained Attentions.** A key component of the proposed method is the local and fine-grained attention that is applied to the selected rich semantic regions. By only processing sub-regions of the images, we can attend to much finer resolutions than would otherwise be possible. The obvious downside of this approach is that the representation lacks global context and dependencies between the attended regions. To that end, we feed the extracted regions to a transformer encoder, which learns global dependencies through the information interaction between the local representations through a **coarse attention** mechanism. Afterward, the [CLS] token of the last transformer is merged with the [CLS] tokens of the first ViT in view of integrating further global context information in the final representation vector. Finally, the resulting token is then passed through a projection head to yield the logits  $\hat{p} \in \mathbb{R}^C$ , where  $C$  is the number of classes. We use a cross-entropy classification loss  $\mathcal{L}_{CE}$  to drive the optimization of our TRoIs model.

**Computational Complexity.** Vision transformers heavily rely on the attention mechanism to learn a high-level

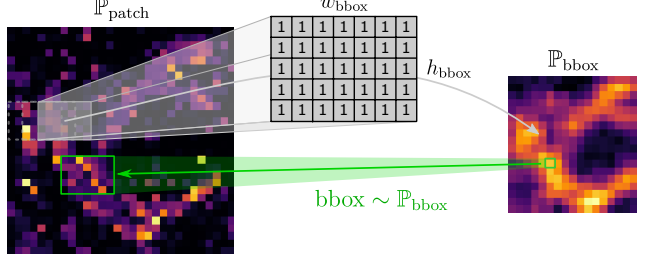


Figure 3. **The bounding box selection scheme for ScoreMix.** The score distribution for each bounding box ( $\mathbb{P}_{\text{bbox}}$ ) is obtained by convolving the patch distribution map  $\mathbb{P}_{\text{patch}}$  with a kernel of **1s** of the bounding box dimensions ( $h_{\text{bbox}}, w_{\text{bbox}}$ ). The bbox is then sampled from  $\mathbb{P}_{\text{bbox}}$ , which we often refer to as  $\mathbb{P}_{\text{source}}$  or  $\mathbb{P}_{\text{target}}$ .

representation from low-level regions. The underlying assumption is that the different sub-regions of the image are not equally important for the overall representation. Despite this key observation, the computation cost dedicated to a sub-region is independent of its contribution to the high-level representation, which is inefficient and undesirable. Our ScoreNet attention mechanism overcomes this drawback by learning to attribute more resources to regions of high interest. For a high-resolution input image  $x_h \in \mathbb{R}^{C \times H \times W}$ , the asymptotical time and memory cost is  $\mathcal{O} \left( \left( \frac{H}{s \cdot P_l} \cdot \frac{W}{s \cdot P_l} \right)^2 \right)$ , when the recommendation stage uses inputs downsampled by a factor  $s$  and processes them with a patch size of  $P_l$ . The derivation of this cost, including that of the recommendation stage, which is independent of the input size can be found in the **Appendix**.

### 3.3. ScoreMix

**Limitations of Concurrent Data Mixing Augmentation.** CutMix [37] randomly mixes samples by cutting a patch region from a source image and pasting it on the target image at the **respective original location** and assumes **uniform distribution** of semantic information, yielding **label misallocation** and **semantic information missing**. Similar to ScoreMix, SaliencyMix [32] introduced the notion of the discriminative regions for cutting and mixing operations. However, SaliencyMix operates under the assumption that the semantic regions are correlated with a high saliency, which typically does not hold for histopathological images. Instead, we propose to alleviate this issue by learning the **distribution of the semantic image regions** using the learned self-attention for [CLS] token of the ViT without requiring architectural changes or additional loss.

More formally, let  $x_s, x_t \in \mathbb{R}^{C \times H \times W}$  be the source and target images respectively and let  $y_s$  and  $y_t$  be their corresponding labels. We aim to mix the source and target samples to generate a new training example  $(x_m, y_m)$ . To do so, we first compute the semantic distributions using the current

parameters of the model and the input samples; namely, we compute  $\mathbb{P}_{\text{source}}(x_s, \theta)$  and  $\mathbb{P}_{\text{target}}(x_t, \theta)$ . Given these distributions and a randomly defined bounding box size, we sample the cutting and pasting locations from the source and target distributions, respectively:

$$\begin{aligned} M_s &\sim \frac{1}{Z_s} \cdot \mathbb{P}_{\text{source}}(x_s, \theta, \lambda) \\ M_t &\sim \frac{1}{Z_t} \cdot (1 - \mathbb{P}_{\text{target}}(x_t, \theta, \lambda)) \end{aligned} \quad (7)$$

where  $Z_s$  and  $Z_t$  are normalization constants, and  $1 - \lambda \sim \mathcal{U}([0, 1])$  defines the strength of the mixing, i.e. the size of the bounding box. The locations of the cutting and pasting regions are encoded as binary masks, i.e.,  $M_s, M_t \in \{0, 1\}^{H \times W}$ , where a value of 1 encodes for a patch in the cutting/pasting region. Under the above formalism, the mixing operation can be defined as:

$$\begin{aligned} x_m &= (\mathbf{1} - M_t) \odot x_t \\ M_t \otimes x_m &\leftarrow M_s \otimes x_s \\ y_m &= \lambda y_t + (1 - \lambda) y_s \end{aligned} \quad (8)$$

where  $\mathbf{1}$  is a mask of ones,  $\odot$  denotes the element-wise multiplication, and  $\otimes$  indicates an indexing w.r.t. a mask.

**Computing the Semantic Distributions.** Computing the semantic distributions of the target and source images is an essential part of the pipeline as it allows for a data-driven selection of the cutting/pasting sites, thereby avoiding the pitfalls of random selection. When the size of the bounding box matches that of a single patch, the distribution can be directly deduced from the self-attention map, as described in Sec. 3.2. As a consequence, and when the bounding box’s size matches that of a single patch, the semantic distribution can be directly obtained from  $\mathbb{P}_{\text{patch}}$  (see Eq. 3). In practice, we would typically use bounding boxes encompassing more than a single patch. In that case, the distribution of the semantic content at the bounding box resolution can be obtained by a local aggregation of the distribution above:

$$\mathbb{P}_{\text{bbox}}(i) \propto \sum_{j \in \mathcal{N}(i)} \mathbb{P}_{\text{patch}}(j) \quad (9)$$

where  $\mathcal{N}(i)$  returns the indices of the patches situated in the bounding box whose top left corner is the patch  $i$ . In practice, this can be efficiently implemented by first unflattening the patch distribution  $\mathbb{P}_{\text{patch}}$ , and convolving it with a kernel of ones and of the same dimension as the desired bounding box (see Fig. 3).

## 4. Experiments

**Datasets.** The primary dataset is the BReAst Carcinoma Sub-typing (*BRACS*) dataset [26]. *BRACS* consists of 4391

RoIs acquired from 325 H&E stained breast carcinoma WSI (at  $0.25 \mu\text{m}/\text{pixel}$ ). The varying dimensions and appearances of the RoIs make for a more authentic but also more challenging dataset. Each RoI is annotated with one of the seven classes: Normal, Benign, Usual Ductal Hyperplasia (UDH), Atypical Ductal Hyperplasia (ADH), Flat Epithelial Atypia (FEA), Ductal Carcinoma In Situ (DCIS), and Invasive. As in [26], we perform training, validation, and test split at the WSI level to avoid test leakage. Our experiments follow the exact splits as [26]. We also use the publicly available BreAst Cancer Histology (*BACH*) dataset [2] to show ScoreNet generalization capabilities. It contains 400 training and 100 testing images from four different breast cancer types: Normal, Benign, In Situ, and Invasive. All images have a fixed size of  $1536 \times 2048$  pixels and a pixel scale of  $0.42 \times 0.42 \mu\text{m}$ . To assess the interpretability of ScoreNet, we further evaluate our model on the *CAMELYON16* dataset [4] for binary tumor classification. We extracted a class-balanced dataset of  $(1920 \times 1920)$  pixels) from high-resolution WSIs.

**Experimental Setup.** We use a modified ViT-tiny architecture [6] (see **Appendix** for more details) and follow exact self-supervised pre-training scheme in [6]. The TRoIs classifier is optimized using the SGD optimizer (momentum=0.9) with a learning rate chosen with the linear scaling rule [13] ( $lr = 10^{-2} \cdot \text{batchsize}/256 = 3.125 \cdot 10^{-4}$ ) annealed with a cosine schedule until  $10^{-6}$ . After pre-training, the ScoreNet’s optimization is performed for 15 epochs with a batch-size of 8. We empirically chose to extract the top  $K = 20$  regions, and a downscaling factor  $s$  is set to 8, cf. **see ablation in the Appendix**. As an image contains on average 238 patches, we thus use less than 10% of the image in our fine-grain stage. All experiments are implemented in PyTorch 1.9 [23] using a single GeForce RTX3070 GPU.

### 4.1. TRoIs Classification Results and Discussion

We first compare our method to existing MIL-based approaches, which aggregate the independent patch-wise representations via the aggregation strategy [22]. The MIL-based methods operate either on multi- or single-scale images such that they benefit from different levels of context and resolution. CNN’s architectures tend to favor texture-based features [12], at the other end of the spectrum are graph neural network-based methods, which model the global dependencies between the local representations and thus rely more on the shape cues. We further compare with graph-based methods with a significant emphasis on HACT-Net [26], which holds the current state-of-art for TRoIs classification on the *BRACS*. ScoreNet reaches a new state-of-the-art weighted F1-score of 64.4% on the *BRACS* TRoIs classification task outperforming HACT-

Table 1. **Comparison of different TRoIs classification methods** using weighted and class-wise F1-scores on the BRACS dataset. The best results are **bold**. A model named ScoreNet/x/y refers to an instance of ScoreNet using the last x [CLS] tokens of the recommendation stage and the last y ones from the aggregation stage.

Method	Normal	Benign	UDH	ADH	FEA	DCIS	Invasive	Weighted F1	
CNN (MIL)	CNN (10×) [22, 29]	48.7 ± 1.7	44.3 ± 1.9	45.0 ± 5.0	24.0 ± 2.8	47.0 ± 4.3	53.3 ± 2.6	86.7 ± 2.6	50.8 ± 2.6
	CNN (20×) [22, 29]	42.0 ± 2.2	42.3 ± 3.1	39.3 ± 2.0	22.7 ± 2.5	47.7 ± 1.2	50.3 ± 3.1	77.0 ± 1.4	46.8 ± 2.2
	CNN (40×) [22, 29]	32.3 ± 4.6	39.0 ± 0.8	23.7 ± 1.7	18.0 ± 0.8	37.7 ± 2.9	47.3 ± 2.0	70.7 ± 0.5	39.4 ± 1.9
	CNN (10× + 20×) [22, 29]	48.3 ± 2.0	45.7 ± 0.5	41.7 ± 5.0	32.3 ± 0.9	46.3 ± 1.4	59.3 ± 2.0	85.7 ± 1.9	52.3 ± 1.9
	CNN (10× + 20× + 40×) [22, 29]	50.3 ± 0.9	44.3 ± 1.2	41.3 ± 2.5	31.7 ± 3.3	51.7 ± 3.1	57.3 ± 0.9	86.0 ± 1.4	52.8 ± 1.9
GNN	CGC-Net [39]	30.8 ± 5.3	31.6 ± 4.7	17.3 ± 3.4	24.5 ± 5.2	59.0 ± 3.6	49.4 ± 3.4	75.3 ± 3.2	43.6 ± 0.5
	Patch-GNN (10×) [3]	52.5 ± 3.3	47.6 ± 2.2	23.7 ± 4.6	30.7 ± 1.8	60.7 ± 5.3	58.8 ± 1.1	81.6 ± 2.2	52.1 ± 0.6
	Patch-GNN (20×) [3]	43.9 ± 4.2	43.4 ± 3.2	19.5 ± 2.3	25.7 ± 2.9	55.6 ± 2.1	52.9 ± 1.8	79.2 ± 1.1	47.1 ± 0.7
	Patch-GNN (40×) [3]	41.7 ± 3.1	32.9 ± 1.0	25.1 ± 3.7	25.6 ± 2.0	49.5 ± 3.5	48.6 ± 4.2	71.6 ± 5.1	43.2 ± 0.6
	TG-GNN [24]	58.8 ± 6.8	40.9 ± 3.0	46.8 ± 1.9	40.0 ± 3.6	63.7 ± 10.5	53.8 ± 3.9	81.1 ± 3.3	55.9 ± 1.0
	CG-GNN [24]	63.6 ± 4.9	47.7 ± 2.9	39.4 ± 4.7	28.5 ± 4.3	72.1 ± 1.3	54.6 ± 2.2	82.2 ± 4.0	56.6 ± 1.3
	CONCAT-GNN	61.0 ± 4.5	43.1 ± 2.3	42.0 ± 4.7	26.1 ± 3.7	71.3 ± 2.1	60.8 ± 3.7	85.4 ± 2.7	57.0 ± 2.3
	HACT-Net [24]	61.6 ± 2.1	47.5 ± 2.9	43.6 ± 1.9	40.4 ± 2.5	74.2 ± 1.4	<b>66.4 ± 2.6</b>	88.4 ± 0.2	61.5 ± 0.9
Ours	Lin. encoder's [CLS]	52.7 ± 9.4	35.6 ± 3.4	34.5 ± 6.7	25.1 ± 3.6	53.5 ± 9.8	38.7 ± 2.8	63.3 ± 7.6	43.8 ± 3.4
	Lin. scorer's [CLS]	57.5 ± 4.2	48.8 ± 5.5	42.7 ± 3.5	42.7 ± 7.4	74.3 ± 5.2	60.5 ± 2.4	90.6 ± 0.2	60.9 ± 3.1
	ScoreNet/4/1	<b>64.6 ± 2.2</b>	52.6 ± 2.8	<b>48.4 ± 2.2</b>	<b>47.4 ± 2.4</b>	77.9 ± 0.7	59.3 ± 1.1	90.6 ± 1.5	64.1 ± 0.7
	ScoreNet/4/3	64.3 ± 1.5	<b>54.0 ± 2.2</b>	45.3 ± 3.4	46.7 ± 1.0	<b>78.1 ± 2.8</b>	62.9 ± 2.0	<b>91.0 ± 1.4</b>	<b>64.4 ± 0.9</b>

Net, by a margin of 2.9% (Table 1). The results are reported for two variants of ScoreNet, namely ScoreNet/4/1 and ScoreNet/4/3, which use the four last [CLS] tokens of the scorer, and the last or the 3 last [CLS] tokens from the coarse attention mechanism (aggregation stage). ScoreNet/4/3 variant puts more emphasis on the features available at (40 $\times$ ), whereas ScoreNet/4/1 is more biased towards the global representation available at (5 $\times$ ) (with a downscaling factor  $s = 8$ ). One can observe that both model variants significantly outperform the existing baseline in terms of weighted F1-scores and for almost every class. More interestingly, the differences in architecture directly translate to differences in the classification results. One could argue that ScoreNet/4/3 is more suitable for classes where the **discriminative features are at the cell level than ScoreNet/4/1, which is more suited when the tissue organization is the discriminative criterion**. Nonetheless, both of these architectures indeed benefit from the information available at each scale. This observation is well supported by the classification results obtained when a linear layer is trained independently on the scorer's or using [CLS] tokens in the aggregation stage. Despite the difference in results between the two model variants, it is clear that they both perform worse when separated, which indicates that the representations of both stages are complementary. In brief, ScoreNet allows for a variety of models, which can be easily tuned to meet prior inductive biases on the ideal scale for a given task.

**ScoreMix & Data-Regime Sensitivity.** We also show that ScoreNet equipped with proposed ScoreMix augmentation achieves superior TRoIs classification performances

Table 2. **The proposed ScoreMix, is compared against CutMix [37], and SaliencyMix [32]** on various fractions of the dataset using identical distribution for the bounding boxes' sizes.

BRACS [%]	No aug.	CutMix	SaliencyMix	ScoreMix
10 %	52.9 $\pm$ 2.4	53.7 $\pm$ 2.9	53.5 $\pm$ 2.7	<b>55.9 <math>\pm</math> 1.9</b>
20 %	57.6 $\pm$ 1.8	58.0 $\pm$ 1.4	57.8 $\pm$ 1.0	<b>58.7 <math>\pm</math> 0.8</b>
50 %	60.4 $\pm$ 1.8	61.2 $\pm$ 2.5	59.8 $\pm$ 2.4	<b>62.3 <math>\pm</math> 0.6</b>
100 %	62.7 $\pm$ 1.6	63.1 $\pm$ 1.1	62.8 $\pm$ 1.2	<b>64.0 <math>\pm</math> 0.7</b>

compared to CutMix and SaliencyMix augmentations for different data regimes, e.g., low-regime with only 10% of the data. **Note that we could beat the state-of-the-art with only 50% of the data and are already on-par or better than most baselines with only 20%.** (Table 2). We argue that these improvements are primarily because our method produces samples with more sensible labels. Indeed, we observe that the regions cut by ScoreMix are, on average, 1.6 $\times$  more discriminative than the regions cut from CutMix or SaliencyMix. Additionally, the regions where the bounding box is pasted on are 0.8 $\times$  times less discriminative when ScoreMix is used than CutMix or SaliencyMix. Our results further support that image saliency used in the SaliencyMix is not correlated with discriminative regions.

**Generalization Capabilities.** To gauge the superior generalization capabilities of our ScoreNet compared to the current SOTA method, HACT-Net [24], we perform an evaluation on datasets, including *CAMELYON16* and *BACH*. Both models are frozen with pre-trained weights on the *BRACS* dataset up to the classification head. To evaluate the quality of features, we either learn a linear classifier on frozen features or apply a  $k$ -nearest-neighbor classifier ( $k = 1$ ) without any finetuning. To evaluate all samples, we per-



Table 3. **Generalization performance of ScoreNet compared to HACT-Net** trained on BRACS and evaluated either on the 400 images of BACH or on 1000 images from CAMELYON16. The weighted F1-scores are presented as the mean and standard deviation over a stratified 5-fold cross-validation fold.

	BRACS $\rightarrow$ BACH		BRACS $\rightarrow$ CAMELYON16	
	Linear	$k$ -NN	Linear	$k$ -NN
<b>ScoreNet</b>	<b>73.4 <math>\pm</math> 3.5</b>	<b>76.9 <math>\pm</math> 6.1</b>	<b>81.1 <math>\pm</math> 3.5</b>	<b>77.0 <math>\pm</math> 4.6</b>
HACT-Net	40.2 $\pm$ 2.8	32.8 $\pm$ 5.8	60.0 $\pm$ 4.6	61.0 $\pm$ 4.2

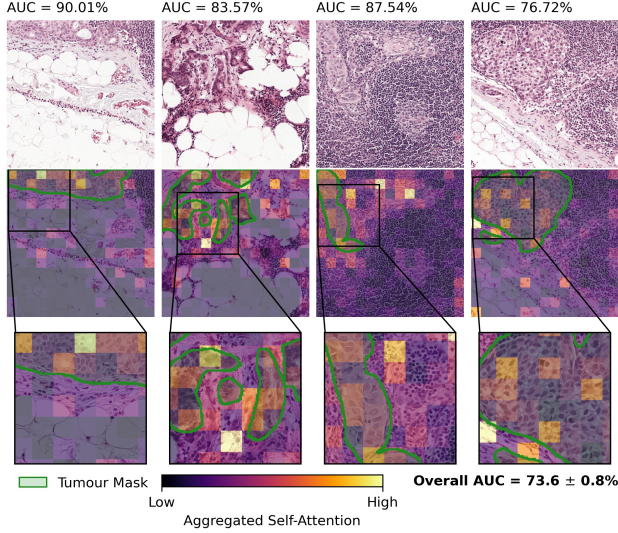


Figure 4. **ScoreNet Interpretability.** Visualization of the semantic distribution, overlaid with the tumour ground truth mask on a few samples of the CAMELYON16 dataset. The ScoreNet is pre-trained on BRACS and fine-tuned on CAMELYON16.

form stratified 5-fold cross-validation. For HACT-Net, we use the available pre-trained weights and follow the code implementation of [26]. As HACT-Net sometimes fails to generate embedding, to have a fair comparison, we only evaluate those samples where HACT-Net could successfully produce embedding (around 95% of the BACH and 80% of CAMELYON16 dataset). Experimental results in Table 3 demonstrate the superiority of ScoreNet in learning generalizable features. It further demonstrates the robustness of ScoreNet regarding the magnification. Indeed, the model is pre-trained on the BRACS at 40 $\times$  magnification while BACH’s images are in the magnifications of 20 $\times$ . Furthermore, the CAMELYON16 dataset contains WSIs collected from lymph nodes in the vicinity of the breast, while BRACS contains WSIs collected by mastectomy or biopsy (i.e., directly in the breast). The excellent knowledge transfer between the two datasets highlights the transferability of features learned by ScoreNet in various use cases.

Table 4. **An Inference throughput comparison of ScoreNet, Vanilla ViT, and HACT-Net** All models were tested with the image size used in the BACH dataset and a single GeForce RTX 3070 GPU filled to its maximum capacity.

	Image size	Throughput (im./s)	Pre-processing
HACT-Net	1536 $\times$ 2048	4.95e-4 $\pm$ 1.40e-3	✓
Vanilla ViT	1536 $\times$ 2048	3.8 $\pm$ 0.1	-
<b>ScoreNet</b>	1536 $\times$ 2048	<b>335.0 <math>\pm</math> 7.9</b>	✗

**Interpretability.** We further show the interpretability of ScoreNet by finetuning the model on CAMELYON16 images using image-level labels only. At test time, we probe the learned semantic distributions of the tumour-positive images. The visualized aggregated attention map in Fig. 4 clearly shows that the models learn to segment to tumour area and interpret **cancer-related morphological information** while never having been constrained to do so. We observe that, on average, 74.6% of the selected 20 patches are tumour-positive.

**Ablation Study on Efficiency.** A key aspect of ScoreNet is its time and computational memory efficiency. We expect a gain of speed compared to the vanilla ViT of the order of the squared downscaling factor (see Appendix for details), typically  $s^2 = 64$ , which is well reflected in practice, as shown in Table 4. Finally, partly due to the self-supervised pre-training, ScoreNet does not require any stain normalization or pre-processing, as opposed to SOTA competitor HACT-Net, which requires both stain normalization and a computationally intensive pre-processing to infer the tissue graph with SLIC [1]. Our method is therefore well suited for real-time application or extension to WSIs.

**Ablation Study on Shape Cues and Robustness.** Here, we investigate whether our ScoreNet’s non-uniform attentions learn to focus on shape-related features? To do so, we design an experiment to study shape cues extracted by the recommendation model via the concatenated [CLS] tokens (Fig. 2). Consequently, we explore the effect of removing the shape information from this part of the architecture. The shape removal is implemented by applying a random permutation of the downsampled image’s tokens at test time. To ensure that only this part is affected by this shape ablation, the downsampled images are passed twice through the recommendation stage; a first time to extract the patches with the original image and a second one with the permuted image to extract the [CLS] tokens. With this setup, a weighted F1-score of 59.8  $\pm$  0.8% is reached, representing a significant drop in performance compared to 64.4  $\pm$  0.9% without permutation. It demonstrates that *i)* the concatenated [CLS] tokens contribute positively to the overall representation and *ii)* the latter is **not permutation invariant** and thus shape-dependent. In a second experiment, we



show that the learned semantic distribution, hence the whole recommendation stage, is also shape-dependent. To that end, we repeat the same experiment, but the patches are extracted from the permuted images, reaching a weighted F1-score of  $59.5 \pm 0.6\%$ . We further observe that for a given image, the overlap of the selected patches with and without permutation is, on average, only 15.7%, which indicates that the semantic distribution learned by ScoreNet is shape-dependent.

## 4.2. Limitations and Potential Negative Impact

The underlying assumption of ScoreNet is that the regions of importance can be inferred from the downsampled images. The latter imposes an upper bound on the downscaling factor and, consequently, on the high-resolution images' size. To adapt ScoreNet to whole slide images, it might be needed to implement a ScoreNet inception, namely using a first ScoreNet to recommend the TRoIs, and a second one to recommend patches from the selected TRoIs. Secondly, ScoreMix, like any other "cut-and-paste"-based augmentation, assumes that the selected regions from the source image are sufficient to infer its label. In some scenarios, the label information may only be available at a larger scale via the shape cues. This issue can be mitigated by using larger bounding boxes.

Finally, a critical point of data-driven algorithms is that they may suffer from biases if the distribution of the training data is itself biased, which may lead to their unfair predictions. In the case of histopathological images, most of the currently available cohorts were acquired in developed countries. Thus, the hereby proposed algorithm could benefit from a more diverse and inclusive training dataset to reduce bias issues in clinical practice.

## 5. Conclusion and Future Work

We propose ScoreNet, a customized transformer-based architecture that learns rich generalizable representations efficiently by leveraging non-uniformity of the semantic content distribution in large histopathological images. Furthermore, we introduce ScoreMix, a data-driven data augmentation method that produces new faithful training samples upon the same key observation. We achieve new SOTA results on the BRACS dataset for TRoIs classification and demonstrate ScoreNet's superior performance for robustness and generalization despite distribution shift on challenging datasets. ScoreNet is not limited to breast cancer and is capable of being potentially extended to other cancer types.

Future work will focus on adapting ScoreNet to WSIs and developing an optimization scheme to directly train ScoreNet in a self-supervised way.

## References

- [1] Radhakrishna Achanta, Appu Shaji, Kevin Smith, Aurelien Lucchi, Pascal Fua, and Sabine Süsstrunk. Slic superpixels compared to state-of-the-art superpixel methods. *IEEE Transactions on Pattern Analysis and Machine Intelligence*, 34(11):2274–2282, 2012. 8
- [2] Guilherme Aresta, Teresa Araújo, Scotty Kwok, Sai Saketh Chennamsetty, Mohammed Safwan, Varghese Alex, Bahram Marami, Marcel Prastawa, Monica Chan, Michael Donovan, et al. Bach: Grand challenge on breast cancer histology images. *Medical image analysis*, 56:122–139, 2019. 6
- [3] Bulut Aygüneş, Selim Aksoy, Ramazan Gökberk Cinbiş, Kemal Kösemehmetoğlu, Sevgen Önder, and Aysegül Üner. Graph convolutional networks for region of interest classification in breast histopathology. In *Medical Imaging 2020: Digital Pathology*, volume 11320, page 113200K. International Society for Optics and Photonics, 2020. 7
- [4] Babak Ehteshami Bejnordi, Mitko Veta, Paul Johannes Van Diest, Bram Van Ginneken, Nico Karssemeijer, Geert Litjens, Jeroen AWM Van Der Laak, Meyke Hermesen, Quirine F Manson, Maschenka Balkenhol, et al. Diagnostic assessment of deep learning algorithms for detection of lymph node metastases in women with breast cancer. *Jama*, 318(22):2199–2210, 2017. 6
- [5] Mathilde Caron, Ishan Misra, Julien Mairal, Priya Goyal, Piotr Bojanowski, and Armand Joulin. Unsupervised learning of visual features by contrasting cluster assignments. In *Thirty-fourth Conference on Neural Information Processing Systems (NeurIPS)*, 2020. 12
- [6] Mathilde Caron, Hugo Touvron, Ishan Misra, Hervé Jégou, Julien Mairal, Piotr Bojanowski, and Armand Joulin. Emerging properties in self-supervised vision transformers. In *Proceedings of the International Conference on Computer Vision (ICCV)*, 2021. 3, 4, 6, 12, 13
- [7] Richard J Chen, Ming Y Lu, Wei-Hung Weng, Tiffany Y Chen, Drew FK Williamson, Trevor Manz, Maha Shady, and Faisal Mahmood. Multimodal co-attention transformer for survival prediction in gigapixel whole slide images. In *Proceedings of the IEEE/CVF International Conference on Computer Vision*, pages 4015–4025, 2021. 3
- [8] Xiangxiang Chu, Bo Zhang, Zhi Tian, Xiaolin Wei, and Huaxia Xia. Do we really need explicit position encodings for vision transformers? *CoRR*, abs/2102.10882, 2021. 14, 15
- [9] Jean-Baptiste Cordonnier, Aravindh Mahendran, Alexey Dosovitskiy, Dirk Weissenborn, Jakob Uszkoreit, and Thomas Unterthiner. Differentiable patch selection for image recognition. In *Proceedings of the IEEE/CVF Conference on Computer Vision and Pattern Recognition*, pages 2351–2360, 2021. 5
- [10] Jia Deng, Wei Dong, Richard Socher, Li-Jia Li, Kai Li, and Li Fei-Fei. Imagenet: A large-scale hierarchical image database. In *2009 IEEE conference on computer vision and pattern recognition*, pages 248–255. Ieee, 2009. 12
- [11] Alexey Dosovitskiy, Lucas Beyer, Alexander Kolesnikov, Dirk Weissenborn, Xiaohua Zhai, Thomas Unterthiner,

- Mostafa Dehghani, Matthias Minderer, Georg Heigold, Sylvain Gelly, Jakob Uszkoreit, and Neil Houlsby. An image is worth 16x16 words: Transformers for image recognition at scale. *ICLR*, 2021. 2, 4
- [12] Robert Geirhos, Patricia Rubisch, Claudio Michaelis, Matthias Bethge, Felix A Wichmann, and Wieland Brendel. Imagenet-trained cnns are biased towards texture; increasing shape bias improves accuracy and robustness. *arXiv preprint arXiv:1811.12231*, 2018. 6
- [13] Priya Goyal, Piotr Dollár, Ross Girshick, Pieter Noordhuis, Lukasz Wesolowski, Aapo Kyrola, Andrew Tulloch, Yangqing Jia, and Kaiming He. Accurate, large minibatch sgd: Training imagenet in 1 hour, 2018. 6
- [14] Le Hou, Dimitris Samaras, Tahsin M Kurc, Yi Gao, James E Davis, and Joel H Saltz. Patch-based convolutional neural network for whole slide tissue image classification. In *Proceedings of the IEEE conference on computer vision and pattern recognition*, pages 2424–2433, 2016. 1, 2
- [15] Maximilian Ilse, Jakub Tomczak, and Max Welling. Attention-based deep multiple instance learning. In *International conference on machine learning*, pages 2127–2136. PMLR, 2018. 1, 2, 4
- [16] Shivam Kalra, Mohammed Adnan, Sobhan Hemati, Taher Dehkharghanian, Shahryar Rahnamayan, and Hamid R Tizhoosh. Pay attention with focus: A novel learning scheme for classification of whole slide images. In *International Conference on Medical Image Computing and Computer-Assisted Intervention*, pages 350–359. Springer, 2021. 2
- [17] Shivam Kalra, Hamid R Tizhoosh, Charles Choi, Sultaan Shah, Phedias Diamandis, Clinton JV Campbell, and Liron Pantanowitz. Yottixel—an image search engine for large archives of histopathology whole slide images. *Medical Image Analysis*, 65:101757, 2020. 2
- [18] Navid Alemi Koohbanani, Balagopal Unnikrishnan, Syed Ali Khurram, Pavitra Krishnaswamy, and Nasir Rajpoot. Self-path: Self-supervision for classification of pathology images with limited annotations. *IEEE Transactions on Medical Imaging*, 2021. 2
- [19] Bin Li, Yin Li, and Kevin W Eliceiri. Dual-stream multiple instance learning network for whole slide image classification with self-supervised contrastive learning. In *Proceedings of the IEEE/CVF Conference on Computer Vision and Pattern Recognition*, pages 14318–14328, 2021. 1, 2, 4
- [20] Chunyuan Li, Jianwei Yang, Pengchuan Zhang, Mei Gao, Bin Xiao, Xiyang Dai, Lu Yuan, and Jianfeng Gao. Efficient self-supervised vision transformers for representation learning. *arXiv preprint arXiv:2106.09785*, 2021. 2
- [21] Oded Maron and Tomás Lozano-Pérez. A framework for multiple-instance learning. *Advances in neural information processing systems*, pages 570–576, 1998. 1, 2
- [22] Caner Mercan, Selim Aksoy, Ezgi Mercan, Linda G Shapiro, Donald L Weaver, and Joann G Elmore. From patch-level to roi-level deep feature representations for breast histopathology classification. In *Medical Imaging 2019: Digital Pathology*, volume 10956, page 109560H. International Society for Optics and Photonics, 2019. 1, 2, 6, 7
- [23] Adam Paszke, Sam Gross, Francisco Massa, Adam Lerer, James Bradbury, Gregory Chanan, Trevor Killeen, Zeming Lin, Natalia Gimelshein, Luca Antiga, et al. Pytorch: An imperative style, high-performance deep learning library. *Advances in neural information processing systems*, 32:8026–8037, 2019. 6
- [24] Pushpak Pati, Maria Frucci, and Maria Gabrani. Hactnet: A hierarchical cell-to-tissue graph neural network for histopathological image classification. In *Uncertainty for Safe Utilization of Machine Learning in Medical Imaging, and Graphs in Biomedical Image Analysis: Second International Workshop, UNSURE 2020, and Third International Workshop, GRAIL 2020, Held in Conjunction with MICCAI 2020, Lima, Peru, October 8, 2020, Proceedings*, volume 12443, page 208. Springer Nature, 2020. 7
- [25] Pushpak Pati, Guillaume Jaume, Antonio Foncubierta, Florinda Feroce, Anna Maria Anniciello, Giosuè Scognamiglio, Nadia Brancati, Maryse Fiche, Estelle Dubruc, Daniel Riccio, et al. Hierarchical cell-to-tissue graph representations for breast cancer subtyping in digital pathology. *arXiv e-prints*, pages arXiv–2102, 2021. 12, 13
- [26] Pushpak Pati, Guillaume Jaume, Antonio Foncubierta-Rodríguez, Florinda Feroce, Anna Maria Anniciello, Giosuè Scognamiglio, Nadia Brancati, Maryse Fiche, Estelle Dubruc, Daniel Riccio, Maurizio Di Bonito, Giuseppe De Pietro, Gerardo Botti, Jean-Philippe Thiran, Maria Frucci, Orcun Goksel, and Maria Gabrani. Hierarchical graph representations in digital pathology. *Medical Image Analysis*, 75:102264, 2022. 2, 6, 8
- [27] David W Romero and Jean-Baptiste Cordonnier. Group equivariant stand-alone self-attention for vision. In *International Conference on Learning Representations*, 2020. 13
- [28] Zhuchen Shao, Hao Bian, Yang Chen, Yifeng Wang, Jian Zhang, Xiangyang Ji, and Yongbing Zhang. Transmil: Transformer based correlated multiple instance learning for whole slide image classification. *arXiv preprint arXiv:2106.00908*, 2021. 3
- [29] Korsuk Sirinukunwattana, Nasullah Khalid Alham, Clare Verrill, and Jens Rittscher. Improving whole slide segmentation through visual context—a systematic study. In *International Conference on Medical Image Computing and Computer-Assisted Intervention*, pages 192–200. Springer, 2018. 2, 7
- [30] Chetan L Srinidhi, Ozan Ciga, and Anne L Martel. Deep neural network models for computational histopathology: A survey. *Medical Image Analysis*, 67:101813, 2021. 1, 2
- [31] Chetan L Srinidhi, Seung Wook Kim, Fu-Der Chen, and Anne L Martel. Self-supervised driven consistency training for annotation efficient histopathology image analysis. *arXiv preprint arXiv:2102.03897*, 2021. 2
- [32] AFM Shahab Uddin, Mst Sirazam Monira, Wheemyung Shin, TaeChoong Chung, and Sung-Ho Bae. Saliencymix: A saliency guided data augmentation strategy for better regularization. In *International Conference on Learning Representations*, 2020. 3, 5, 7
- [33] Ashish Vaswani, Noam Shazeer, Niki Parmar, Jakob Uszkoreit, Llion Jones, Aidan N Gomez, Łukasz Kaiser, and Illia Polosukhin. Attention is all you need. In *Advances in neural information processing systems*, pages 5998–6008, 2017. 2

- [34] Devesh Walawalkar, Zhiqiang Shen, Zechun Liu, and Marios Savvides. Attentive cutmix: An enhanced data augmentation approach for deep learning based image classification. In *ICASSP 2020-2020 IEEE International Conference on Acoustics, Speech and Signal Processing (ICASSP)*, pages 3642–3646. IEEE, 2020. [2](#), [3](#)
- [35] Xiyue Wang, Sen Yang, Jun Zhang, Minghui Wang, Jing Zhang, Junzhou Huang, Wei Yang, and Xiao Han. Transpath: Transformer-based self-supervised learning for histopathological image classification. In *International Conference on Medical Image Computing and Computer-Assisted Intervention*, pages 186–195. Springer, 2021. [2](#), [3](#)
- [36] Yan Xu, Zhipeng Jia, Yuqing Ai, Fang Zhang, Maode Lai, I Eric, and Chao Chang. Deep convolutional activation features for large scale brain tumor histopathology image classification and segmentation. In *2015 IEEE international conference on acoustics, speech and signal processing (ICASSP)*, pages 947–951. IEEE, 2015. [2](#)
- [37] Sangdoo Yun, Dongyoon Han, Seong Joon Oh, Sanghyuk Chun, Junsuk Choe, and Youngjoon Yoo. Cutmix: Regularization strategy to train strong classifiers with localizable features. In *Proceedings of the IEEE/CVF International Conference on Computer Vision*, pages 6023–6032, 2019. [2](#), [3](#), [5](#), [7](#)
- [38] Hongyi Zhang, Moustapha Cisse, Yann N. Dauphin, and David Lopez-Paz. mixup: Beyond empirical risk minimization. *International Conference on Learning Representations*, 2018. [3](#)
- [39] Yanning Zhou, Simon Graham, Navid Alemi Koohbanani, Muhammad Shaban, Pheng-Ann Heng, and Nasir Rajpoot. Cgc-net: Cell graph convolutional network for grading of colorectal cancer histology images. In *Proceedings of the IEEE/CVF International Conference on Computer Vision Workshops*, pages 0–0, 2019. [2](#), [7](#)

## A. Appendix Overview

In this appendix, we provide additional details and materials. The remaining of this section is organized as follows. In Sec. B we detail the architectural and training meta-parameters choices. Additional ablations experiments are detailed in Sec. C. A detailed derivation of the computational cost is proposed in Sec. D. Finally, we discuss in Sec. E some properties of ScoreMix and present some examples of ScoreMixed samples.

## B. Experimental Setup & Datasets

### B.1. Networks Architectures

The ScoreNet comprises three essential modules: the recommendation stage and the fine and coarse-grained attention mechanisms. The recommendation stage and the fine-grained attention mechanism rely on an identical network backbone: a modified tiny ViT. The following parameters were modified to be tailored for the task:

- `embed_dim=96`.
- `depth=8`.
- `num_heads=4`.
- `mlp_ratio=2`.

These modifications were brought to allow for a self-supervised pre-training with a sufficiently large batch size ( $bs \geq 128$ ), which was reported to be of significant importance to reach good performance [6]. The coarse attention mechanism aggregates the representations of the  $K$  most semantically relevant regions via a transformer encoder with the following parameters:

- `embed_dim=96`.
- `depth=5`.
- `num_heads=4`.
- `mlp_ratio=2`.

### B.2. Self-Supervised Pre-training

Our modular architecture allows for independent self-supervised pre-trainings of the recommendation stage and fine-grained attention modules. We follow the method of [6] as closely as possible. Apart from the difference in architectures described in Sec. B.1, we made minor modifications in the projection head to account for the reduced heterogeneity in our datasets compared to ImageNet [10]. The modified parts are:

- `hidden_dim=1024`.
- `bottleneck_dim=128`.
- `out_dim=1024`.

These modifications are in line with the interpretation of [5] which considers the last linear as a projection on a set of

learnable centroids and that their number should be adapted to avoid empty clusters. This interpretation is particularly well suited when both the last layer’s input and weight are normalized, which is the case in our setup. The remaining parameters, aside from the position encoding which is discussed in Sec. C, are set to the default value (see [6] for details).

### B.3. Datasets

We extract two auxiliary datasets from the BRACS dataset [25]: a tile dataset at  $40\times$  and a low-resolution thumbnail dataset at  $\frac{40}{s}\times$ , where  $s$  is the down-scaling ratio. The former dataset is used to pre-train the fine-grained attention module, whereas the latter serves to pre-train the recommendation stage. We experimented with two variants of these paired datasets. The first variant is designed for a version of ScoreNet where the dimension of the finely attended regions is  $P_h = 224$ , the recommendation stage processes low-resolution patches of dimension  $P_l = 16$  and consequently a down-scaling ratio  $s = 14$ . The second variant is designed for a version of ScoreNet where the dimension of the finely attended regions is  $P_h = 128$ , the recommendation stage processes low-resolution patches of dimension  $P_l = 16$  and consequently a down-scaling ratio  $s = 8$ . Each of these datasets are extracted from the WSIs available in the BRACS dataset using an overlap of 0.5, and each contains approximately  $150k$  images for a fair comparison of the two variants (Sec. C)

An additional tile dataset is extracted from CAMELYON16, which is, to our knowledge, the only one with patch-level annotations. This dataset is used to evaluate the pre-training of the fine-grained attention module. The latter is composed of  $10k$  images at  $40\times$ , of dimensions  $128 \times 128$  or  $224 \times 224$ . It is class-balanced, and any patch which contains tumorous tissue is considered tumour positive. This dataset is also used to measure the effectiveness of the position encoding on the fine-grained attention module in Sec. C.

## C. Additional Ablations

**Down-Scaling Ratio & Dimensions of the Attended Regions.** A key component of the proposed pipeline is to determine the down-scaling ratio,  $s$ , and the dimension of the square patches in low resolution,  $P_l \times P_l$ , and in high resolution,  $P_h \times P_h$ . Considering the well-studied nature of the ViTs scorers, we use the standard patch dimension  $P_l = 16$  for the patches in low resolution. It has been shown that smaller patches ( $P_l = 8$  or  $P_l = 5$ ) improve the quality of the learned representations [6], nonetheless the incurred increase in computational and memory cost is unsuitable for our application. For the high-resolution patches, we experiment with two standard patch dimensions:  $P_h = 128$  and  $P_h = 224$ . As the self-attention of the recommenda-



Table 5. **A weighted  $k$  Nearest Neighbors classifier assesses the learned features’ discriminability (weighted F1-score) on the low-resolution BACH dataset.** The performances of CNN and ViT-based architectures are compared, and similarly for two down-scaling ratios ( $s = 8$  or  $s = 14$ ). A 4-fold approach with 75%/25% train/test splits is used.

$k$	ViT				CNN			
	Teacher		Student		Teacher		Student	
	$s = 14$	$s = 8$	$s = 14$	$s = 8$	$s = 14$	$s = 8$	$s = 14$	$s = 8$
1	71.7 $\pm$ 6.4	<b>78.5 <math>\pm</math> 6.4</b>	73.6 $\pm$ 5.1	77.4 $\pm$ 5.1	63.6 $\pm$ 5.1	64.4 $\pm$ 1.9	63.8 $\pm$ 3.2	63.9 $\pm$ 2.2
5	71.5 $\pm$ 1.7	<b>81.7 <math>\pm</math> 3.2</b>	72.8 $\pm$ 1.9	81.0 $\pm$ 4.0	65.1 $\pm$ 3.3	64.7 $\pm$ 2.1	64.1 $\pm$ 4.6	65.4 $\pm$ 2.7
10	71.9 $\pm$ 2.4	77.8 $\pm$ 2.8	72.5 $\pm$ 2.5	<b>77.9 <math>\pm</math> 3.4</b>	62.0 $\pm$ 3.8	58.9 $\pm$ 2.9	61.5 $\pm$ 5.8	61.1 $\pm$ 2.5
20	71.3 $\pm$ 4.0	76.3 $\pm$ 3.0	72.5 $\pm$ 3.0	<b>76.5 <math>\pm</math> 4.0</b>	64.0 $\pm$ 6.7	55.5 $\pm$ 1.8	61.0 $\pm$ 9.2	55.4 $\pm$ 2.4
50	71.2 $\pm$ 4.0	<b>74.7 <math>\pm</math> 4.7</b>	70.9 $\pm$ 3.3	74.3 $\pm$ 5.7	59.3 $\pm$ 5.3	56.1 $\pm$ 3.2	58.1 $\pm$ 6.2	54.6 $\pm$ 3.9
100	71.7 $\pm$ 4.1	<b>74.0 <math>\pm</math> 5.5</b>	71.4 $\pm$ 3.8	73.6 $\pm$ 5.9	57.4 $\pm$ 3.4	50.6 $\pm$ 5.1	56.2 $\pm$ 3.0	48.7 $\pm$ 4.7

Table 6. **A weighted  $k$  Nearest Neighbors classifier assesses the learned features’ discriminability (weighted F1-score) on the low-resolution BRACS dataset.** The performances of CNN and ViT-based architectures are compared, and similarly for two down-scaling ratios ( $s = 8$  or  $s = 14$ ). The  $k$ -NN classifier is trained on the merged train/valid set and evaluated on the test set (see [25]), hence the high performances.

$k$	ViT				CNN			
	Teacher		Student		Teacher		Student	
	$s = 14$	$s = 8$	$s = 14$	$s = 8$	$s = 14$	$s = 8$	$s = 14$	$s = 8$
1	52.5	54.3	51.6	<b>55.0</b>	45.2	45.5	45.4	44.7
5	55.2	<b>56.1</b>	55.4	55.8	47.1	47.6	46.6	46.2
10	57.2	56.4	<b>57.5</b>	56.7	49.3	46.5	50.5	45.8
20	56.9	58.0	<b>58.1</b>	57.6	47.1	47.6	45.9	47.0
50	56.2	<b>57.5</b>	55.7	56.9	41.2	44.9	40.6	44.9
100	53.9	54.0	<b>54.3</b>	53.7	40.3	43.5	40.1	44.2

tion stage is used as a learnable distribution of the semantic content, there should exist a 1-to-1 mapping between the low-resolution patches and the high-resolution regions that can be extracted. As a consequence, the down-scaling ratio is fully determined by the dimensions of the patches:  $s = P_h/P_l$ . In our case, it translates to down-scaling ratio of either  $s = 8$ , or  $s = 14$ .

To find out which of these two setups is the most suitable for our application, we compare the models obtained by each of them via a weighted  $k$  Nearest Neighbours classifier, which has the advantage of being fast and not requiring any finetuning. In Table 6, we compare the classification results on the low-resolution ( $\frac{40}{s} \times$ ) BRACS dataset. We report the results of both the teacher and the student models as well as those obtained by a CNN with comparable capacity and identical pre-training. We do not observe significant differences between the two scales. These differences are, on the other hand, much more emphasized when evaluating the same models on the low-resolution ( $\frac{20}{s} \times$ ) BACH dataset (see Table 5). These promising results on the BACH dataset, despite the scale mismatched, are to be credited to

the local to global views pre-training method [6].

The quality of the fine-grained attention module is assessed with the aforementioned method on the tile CAMELYON16 dataset introduced in Sec. B.3, and the hereby obtained results are reported in Table 7. In conclusion, we observe that the difference is either marginal (Table 6 & 7) or significantly in favor of the setup where  $s = 8$  (Table 5) and therefore chose this setup for the remaining experiments and architectures. As a side note, the CNN architecture performs substantially worth, but it is most likely due to the fact that the DINO [6] method is biased towards ViT architectures, and thus we do not extend our researches in that direction.

**Positional Encoding.** Without position encoding (PE), a ViT processes token as a set and hence completely discards the global shape information; therefore, position encoding is essential. The common approach is to learn a single matrix of absolute and additive position encoding jointly during the training phase. This method suffers to drawbacks: *i*) the absolute encoding of each token’s position implies that a pattern is different at every location it occurs, which reduces the sample efficiency [27], and *ii*) as a consequence of the storage of the position encoding in a single matrix, the model treats the input tokens as a 1D sequence and thus mislays the multi-dimensionality of the inputs. The latter is not an issue as long as the input images have the same aspect ratio, as is the case with the local/global crops strategy of DINO [6]. Nonetheless, and as depicted in Fig. 5, this approach fails when the model is fed an image of a different aspect ratio than those used to train the position encoding. As illustrated in Fig. 5, the 2D sine-cos does not introduce any artifacts when used with images of different resolutions. On the other hand, any absolute position encoding is not a translation equivariant operation, which is an undesired property for planar images. For these reasons, we experiment with Conditional Position encoding Vision

Table 7. A weighted  $k$  Nearest Neighbors classifier assesses the discriminability (weighted F1-score) of the learned features on the tile CAMELYON16 dataset (see Sec. B.3). The performances of CNN and ViT-based architectures is compared, and similarly for two tile dimensions ( $128 \times 128$  and  $224 \times 224$ ) corresponding to down-scaling ratios of  $s = 8$  and  $s = 14$ , respectively. A 4-fold approach with 75%/25% train/test splits is used.

$k$	ViT				CNN			
	Teacher		Student		Teacher		Student	
	$s = 14$	$s = 8$	$s = 14$	$s = 8$	$s = 14$	$s = 8$	$s = 14$	$s = 8$
1	$89.7 \pm 0.6$	$89.1 \pm 0.4$	<b><math>89.6 \pm 0.6</math></b>	$89.1 \pm 0.4$	$87.0 \pm 0.8$	$85.8 \pm 1.1$	$87.2 \pm 0.9$	$85.8 \pm 0.8$
5	<b><math>91.7 \pm 0.4</math></b>	$91.1 \pm 0.5$	$91.6 \pm 0.3$	$91.2 \pm 0.6$	$89.9 \pm 1.7$	$88.8 \pm 1.8$	$89.8 \pm 1.7$	$88.7 \pm 1.7$
10	<b><math>91.9 \pm 0.5</math></b>	$91.4 \pm 0.5$	<b><math>91.9 \pm 0.5</math></b>	$91.5 \pm 0.4$	$90.3 \pm 1.0$	$89.0 \pm 0.5$	$90.2 \pm 1.1$	$89.0 \pm 0.6$
20	<b><math>91.6 \pm 0.6</math></b>	$91.2 \pm 0.3$	<b><math>91.6 \pm 0.4</math></b>	$91.2 \pm 0.4$	$90.0 \pm 1.1$	$89.0 \pm 0.5$	$89.8 \pm 1.1$	$88.9 \pm 0.6$
50	<b><math>91.4 \pm 0.9</math></b>	$90.7 \pm 0.6$	$91.3 \pm 1.0$	$90.7 \pm 0.5$	$88.8 \pm 1.1$	$88.6 \pm 0.8$	$88.9 \pm 1.1$	$88.5 \pm 0.8$
100	<b><math>90.9 \pm 1.1</math></b>	$90.1 \pm 0.6$	<b><math>90.9 \pm 1.1</math></b>	$90.0 \pm 0.5$	$88.2 \pm 1.0$	$87.6 \pm 1.0$	$88.1 \pm 1.0$	$87.6 \pm 0.9$

Table 8. A weighted  $k$  Nearest Neighbors classifier assesses the learned features’ discriminability (weighted F1-score) on the low-resolution BACH and BRACS datasets. A fixed and absolute PE (2D sine-cos)’s performances are compared to a learnable and conditional PE (CPVT and CPVT-GAP). The  $k$ -NN classifier is trained on the merged train/valid set and evaluated on the test set (BRACS), and a 4-fold approach with 75%/25% train/test splits is used for BACH dataset.

$k$	BACH						BRACS					
	2D sine-cos		CPVT		CPVT-GAP		2D sine-cos		CPVT		CPVT-GAP	
	Teacher	Student	Teacher	Student	Teacher	Student	Teacher	Student	Teacher	Student	Teacher	Student
1	$76.0 \pm 3.4$	$75.0 \pm 4.0$	$76.6 \pm 2.9$	$77.7 \pm 2.0$	<b><math>78.5 \pm 6.4</math></b>	$77.4 \pm 5.1$	$42.2$	$42.3$	$49.6$	$49.2$	$54.3$	<b><math>55.0</math></b>
5	$74.6 \pm 4.2$	$75.6 \pm 4.2$	$76.8 \pm 3.0$	$76.3 \pm 3.7$	<b><math>81.7 \pm 3.2</math></b>	$81.0 \pm 4.0$	$45.3$	$45.7$	$53.3$	$53.2$	<b><math>56.1</math></b>	$55.8$
10	$76.3 \pm 4.1$	$75.6 \pm 4.6$	$76.3 \pm 5.0$	$76.0 \pm 5.2$	$77.8 \pm 2.8$	<b><math>77.9 \pm 3.4</math></b>	$47.2$	$46.3$	$54.3$	$54.5$	$56.4$	<b><math>56.7</math></b>
20	$73.9 \pm 3.5$	$73.9 \pm 3.5$	$75.7 \pm 5.3$	$72.9 \pm 5.8$	$76.3 \pm 3.0$	<b><math>76.5 \pm 4.0</math></b>	$48.2$	$47.6$	$53.3$	$51.5$	<b><math>58.0</math></b>	$57.6$
50	$73.5 \pm 4.3$	$73.0 \pm 4.1$	$74.2 \pm 5.1$	$73.4 \pm 6.5$	<b><math>74.7 \pm 4.7</math></b>	$74.3 \pm 5.7$	$47.0$	$47.3$	$50.8$	$49.7$	<b><math>57.5</math></b>	$56.9$
100	$72.8 \pm 3.7$	$73.0 \pm 3.1$	$73.6 \pm 5.8$	$71.4 \pm 7.4$	<b><math>74.0 \pm 5.5</math></b>	$73.6 \pm 5.9$	$45.5$	$45.0$	$48.4$	$48.1$	<b><math>54.0</math></b>	$53.7$

Transformer (CPVT) [8]. This PE is input-dependent and convolution-based; as a consequence, it is suitable for any input resolution and patch-wise translation-equivariant. Interestingly, Fig. 6 reveals that the PE of border tokens is slightly different due to the needed zero-padding. This finding is in-line with the authors’ claim that the absolute position encoding can be inferred from zero-paddings [8]. We are under the impression that CPVT is well suited to be used conjointly with ScoreMix as the local processing of the token is convenient for detecting local discontinuity caused by the pasting operation, which is needed to incorporate the added content to the global representation (see Sec. E). In Table 8 and Table 9 we evaluate the discriminability of the features obtained by a pre-training under the DINO framework and with various position encoding methods. Table 9, which reports results on the tile CAMELYON16 dataset (see Sec. B.3), does not provide substantial shreds of evidence in favor of one PE or the other; we postulate that this lack of significant differences is due to the lessened importance of position encoding for the tile dataset.

Indeed, at  $40\times$  and with tiles of dimension  $128 \times 128$ , the available features are mostly texture-based and the relative organization of the patches is less relevant. This

claim is well supported by the substantial differences in performance obtained by distinct PE when evaluated on the low-resolution BACH and BRACS datasets (see Table 9). These differences are further exacerbated by the fact that images on which performance is evaluated are either of varied size (BRACS) or at least of a different dimension than those used during the pre-training (BACH). Notably, there seems to be a significant performance discrepancy between the models using a [CLS] token (CPVT) and those based on a global average pooling (CPVT-GAP). Based on these results, we select the CPVT-GAP method for the remaining experiments. Note that throughout this text we referred to [CLS] token when actually referring to a GAP token. Additionally, we have slightly modified the method to be able to extract one self-attention map per transformer head: instead of performing the GAP operation after the very last layer of the transformer encoder, we do it after the  $(L - 1)^{th}$  layer and concatenate the resulting token to the sequence, thereby producing a pseudo [CLS] token. Similarly, when  $m$  pseudo [CLS] tokens are used, this operation is performed after the  $(L - m)^{th}$  layer.

Table 9. A weighted  $k$  Nearest Neighbors classifier assesses the discriminability (weighted F1-score) of the learned features on the tile CAMELYON16 dataset (see Sec. B.3). A fixed and absolute PE (2D sine-cos)’s performances are compared to a learnable and conditional PE (CPVT and CPVT-GAP). A 4-fold approach with 75%/25% train/test splits is used.

$k$	2D sine-cos		CPVT		CPVT-GAP	
	Teacher	Student	Teacher	Student	Teacher	Student
1	$88.2 \pm 0.9$	$88.4 \pm 0.6$	$88.8 \pm 0.4$	$88.8 \pm 0.4$	<b><math>89.1 \pm 0.4</math></b>	$89.1 \pm 0.4$
5	$91.1 \pm 0.9$	$91.0 \pm 1.0$	$90.9 \pm 0.5$	$90.9 \pm 0.6$	$91.1 \pm 0.5$	<b><math>91.2 \pm 0.6</math></b>
10	$91.2 \pm 0.7$	$91.2 \pm 0.5$	$91.1 \pm 0.4$	$91.1 \pm 0.3$	$91.4 \pm 0.5$	<b><math>91.5 \pm 0.4</math></b>
20	$91.1 \pm 0.7$	$91.1 \pm 0.6$	$91.3 \pm 0.5$	<b><math>91.4 \pm 0.5</math></b>	$91.2 \pm 0.3$	$91.2 \pm 0.4$
50	$90.5 \pm 0.7$	$90.6 \pm 0.7$	<b><math>90.8 \pm 0.6</math></b>	<b><math>90.8 \pm 0.5</math></b>	$90.7 \pm 0.6$	$90.7 \pm 0.5$
100	<b><math>90.2 \pm 1.8</math></b>	<b><math>90.2 \pm 0.8</math></b>	<b><math>90.2 \pm 0.6</math></b>	<b><math>90.2 \pm 0.6</math></b>	$90.1 \pm 0.6$	$90.0 \pm 0.5$

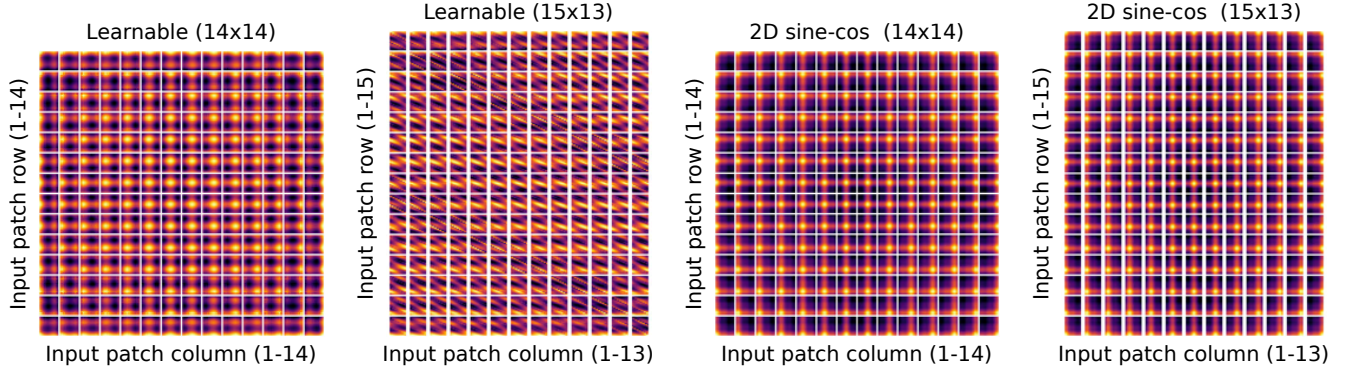


Figure 5. The cosine similarity of a learnable and 2D sine-cos positional encoding is compared. The learnable positional encoding introduces undesirable artifacts when the aspect ratio changes (*Learnable (15x13)*).

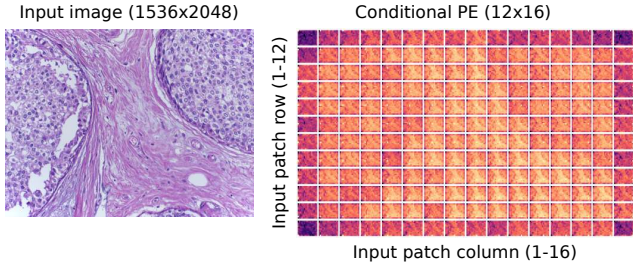


Figure 6. The conditional position encoding [8] of a non-squared input image is represented. The PE is image-dependent and captures the local interactions between tokens.

### C.1. ScoreNet under the Magnifying Glass

**Just a Glorified Low-resolution ViT?** We explore the usage of high-resolution images for predictions. For that purpose, we mask, at test time, 75% of the selected high-resolution regions and report the hereby obtained results in Table 10. As expected, we observe that the ScoreNet/4/3 variant uses the high-resolution content more. Furthermore, these results shed light on how the high-resolution information is not equally relevant for each class. An interesting property that was found through this experiment is that

for each variant of ScoreNet, the higher the performance of a given model is, the more it is affected by the removal of the high-resolution information (see Table 11). Differently stated, **the models which perform the best are the ones that rely the most on the high-resolution information**. Despite that, we expected a more considerable drop of performance from this masking operation, which begs the question; *is ScoreNet nothing but a glorified low-resolution ViT?* To answer that question, we train the exact same ViT as the one used in the recommendation stage and the same setting, but basing the predictions solely based on the scorer’s [CLS] tokens and hence without the feedback from the high-resolution stage. Table 12 clearly shows a gap of almost 10% compared to ScoreNet’s results and, more interestingly, a gap of more than 5% when compared to the exact same ViT, but trained with the high-resolution feedback. The above results seem to **indicate that some sort of high-resolution information distillation occurs during the training of ScoreNet**.

### D. Computational Cost

Vision transformers heavily rely on the attention mechanism to learn a high-level representation from low-level re-

Table 10. **At test time, 75% of the selected high-resolution regions are randomly masked.** ScoreNet/4/1 and ScoreNet/4/3 do not equally rely on the high-resolution content.

Masking	Normal	Benign	UDH	ADH	FEA	DCIS	Invasive	Weighted F1
ScoreNet/4/1	<b>64.6 ± 2.2</b>	<b>52.6 ± 2.8</b>	<b>48.4 ± 2.2</b>	<b>47.4 ± 2.4</b>	77.9 ± 0.7	59.3 ± 1.1	<b>90.6 ± 1.5</b>	<b>64.1 ± 0.7</b>
Masked ScoreNet/4/1	61.1 ± 2.7	50.8 ± 1.4	45.9 ± 2.2	41.0 ± 3.5	<b>78.8 ± 0.5</b>	<b>59.9 ± 3.3</b>	<b>90.6 ± 1.1</b>	62.4 ± 0.6
ScoreNet/4/3	64.3 ± 1.5	<b>54.0 ± 2.2</b>	<b>45.3 ± 3.4</b>	<b>46.7 ± 1.0</b>	<b>78.1 ± 2.8</b>	<b>62.9 ± 2.0</b>	<b>91.0 ± 1.4</b>	<b>64.4 ± 0.9</b>
Masked ScoreNet/4/3	<b>64.9 ± 2.4</b>	51.7 ± 0.5	44.4 ± 4.0	22.0 ± 6.2	77.6 ± 1.0	60.8 ± 1.6	87.2 ± 1.3	59.6 ± 0.7

Table 11. **The performance drop incurred by the high-resolution masking operation of individual models is monitored.** The models that rely the most on the high-resolution content are the ones that perform the best.

ScoreNet/4/1			ScoreNet/4/3		
63.3	$\xrightarrow{-0.6}$	62.7 ± 0.2	63.3	$\xrightarrow{-2.8}$	60.5 ± 0.1
63.8	$\xrightarrow{-2.2}$	61.6 ± 0.1	64.8	$\xrightarrow{-5.2}$	59.6 ± 0.3
64.9	$\xrightarrow{-2.2}$	62.7 ± 0.3	65.0	$\xrightarrow{-6.4}$	58.6 ± 0.3

regions. The underlying assumption is that the different sub-regions of the image are not equally important for the overall representation. Despite this key observation, the computation cost dedicated to a sub-region is independent of its contribution to the high-level representation, which is inefficient and undesirable. Our ScoreNet attention mechanism overcomes this drawback by learning to attribute more resources to regions of high interest. Let us consider a high resolution input image  $x_h \in \mathbb{R}^{C \times H \times W}$ , a low resolution version of the image  $x_l \in \mathbb{R}^{C \times h \times w}$  is obtained by applying a down-scaling of a factor  $s$ , namely  $h = H/s$  and  $w = W/s$ . The low-resolution image is fed to a scorer model (recommendation stage), which recommends the regions where to apply fine-grained attention. If this operation is implemented by a ViT, its computational cost is  $\mathcal{O}\left(\left(\frac{h}{P_l} \cdot \frac{w}{P_l}\right)^2\right)$  with  $P_l$  is the dimension of the patches in low resolution. Using a ViT as the scorer model, there is a one-to-one mapping between the low-resolution patches and the regions the model can process with fine-grained attention; as a consequence, the dimension of the regions is  $P_h = s \cdot P_l$ . Attending to such regions with a patch size,  $P_a$ , has a computational cost of  $\mathcal{O}\left(\left(\frac{P_h}{P_a} \cdot \frac{P_h}{P_a}\right)^2\right)$  and the model processes  $k$  of them, hence  $\mathcal{O}\left(k \cdot \left(\frac{P_h}{P_a} \cdot \frac{P_h}{P_a}\right)^2\right)$ . Finally, a coarse attention mechanism is applied to endow the locally attended regions with contextual information. This final step costs  $\mathcal{O}(k^2)$ . On the other hand, a vanilla ViT would attend uniformly across the whole image with a cost of  $\mathcal{O}\left(\left(\frac{H}{P_a} \cdot \frac{W}{P_a}\right)^2\right)$ . Importantly, we observe that only the

recommendation stage’s cost depend on the input size; consequently, if this step is implemented as a ViT and with a down-scaling ratio  $s \in [8, 14]$  the asymptotic cost is reduced by approximately two orders of magnitude, as we typically used  $P_a = P_l$  in practice. At last, one can observe that the asymptotic cost can be made linear w.r.t. the input dimension by adopting a convolution-based architecture for the recommendation stage.

## E. ScoreMix Investigation & Examples

The underlying assumption of the “cut-and-paste”-based augmentation methods is that the trained model can assimilate and incorporate the pasted region to the representation of the target image. In the case of ScoreNet, it translates to attending to the pasted area in low or high resolution. Fig. 7 depicts an example of ScoreNet being able to detect and localize the pasted regions even when the latter is small and hard to distinguish. We further observe that a local change in the image directly affects the global representations as the representation of each token is adapted to accommodate the local change in information. This behavior would typically not be observed in a CNN-based architecture until the very last layers. Fig. 7 further highlights the ability of ScoreMix to treat images of different dimensions and aspect ratio.



Table 12. The recommendation stage’s ViT is trained without receiving any feedback from the high-resolution-based predictions. Its features discriminability is significantly worth than that of the same model but trained jointly with the high-resolution stage.

Model	Normal	Benign	UDH	ADH	FEA	DCIS	Invasive	Weighted F1
ViT	$53.3 \pm 2.8$	$42.8 \pm 1.9$	$37.1 \pm 2.9$	$32.4 \pm 2.4$	$77.3 \pm 0.2$	$51.2 \pm 1.3$	$85.0 \pm 1.8$	$55.5 \pm 0.1$
Lin. scorer’s [CLS]	$57.5 \pm 4.2$	$48.8 \pm 5.5$	$42.7 \pm 3.5$	$42.7 \pm 7.4$	$74.3 \pm 5.2$	$60.5 \pm 2.4$	$90.6 \pm 0.2$	$60.9 \pm 3.1$
ScoreNet/4/1	<b><math>64.6 \pm 2.2</math></b>	$52.6 \pm 2.8$	<b><math>48.4 \pm 2.2</math></b>	<b><math>47.4 \pm 2.4</math></b>	$77.9 \pm 0.7$	$59.3 \pm 1.1$	$90.6 \pm 1.5$	$64.1 \pm 0.7$
ScoreNet/4/3	$64.3 \pm 1.5$	<b><math>54.0 \pm 2.2</math></b>	$45.3 \pm 3.4$	$46.7 \pm 1.0$	<b><math>78.1 \pm 2.8</math></b>	<b><math>62.9 \pm 2.0</math></b>	<b><math>91.0 \pm 1.4</math></b>	<b><math>64.4 \pm 0.9</math></b>

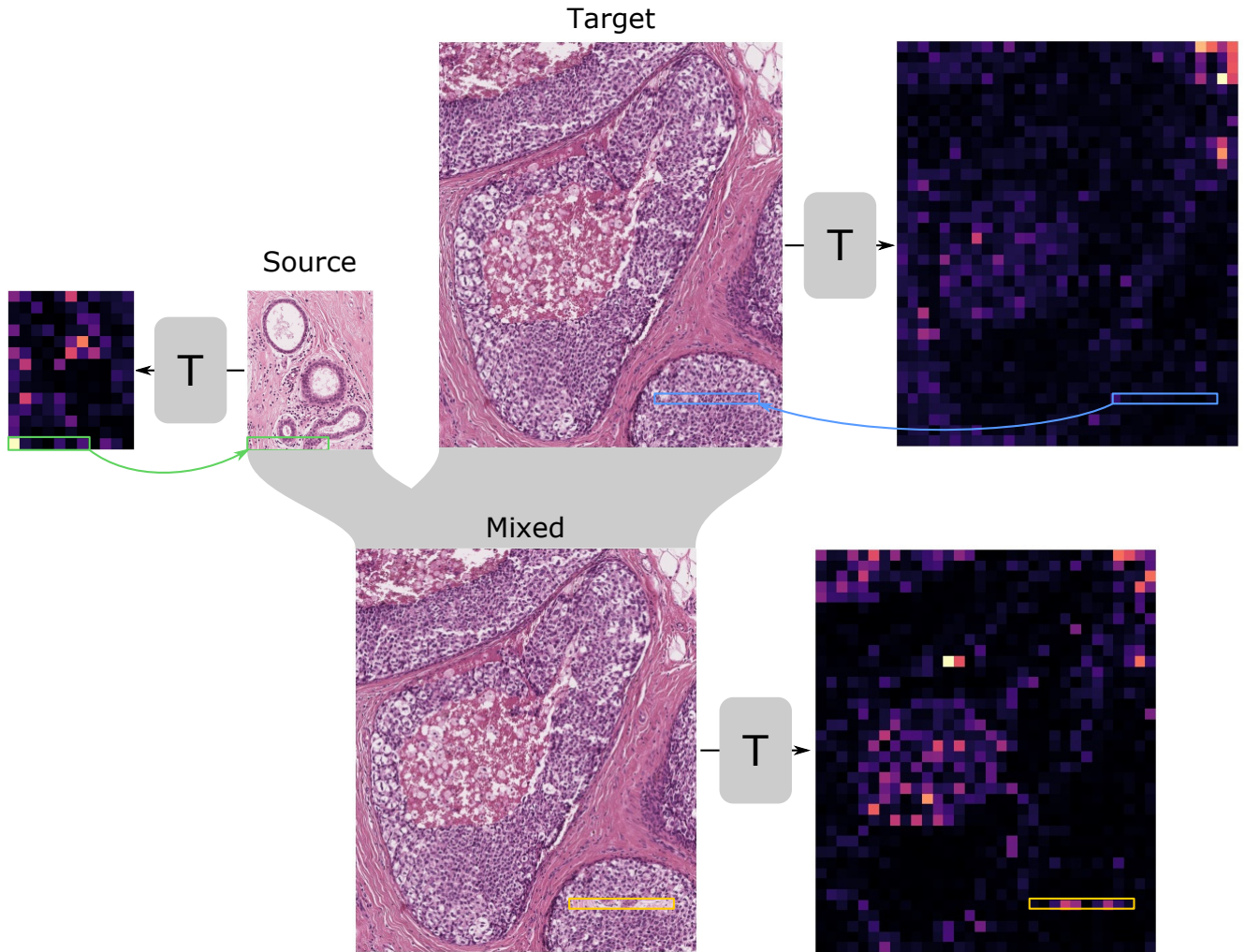


Figure 7. The learned semantic distribution can detect and localize the newly pasted content. The green box highlights the region pasted from the source to the target image. The blue box represents the region where the new content is pasted. The yellow box highlights the modified region in the mixed image.  $T$  represents the scorer network of ScoreNet.